Published in final edited form as:

IEEE Trans Med Imaging. 2013 October ; 32(10): 1765–1776. doi:10.1109/TMI.2013.2264062.

Wall-Motion Based Analysis of Global and Regional Left Atrial Mechanics

Christian B. Moyer[1], **Patrick A. Helm**[2], **Christopher J. Clarke**[3], **Loren P. Budge**[4], **Christopher M. Kramer**[5,6], **John D. Ferguson**[6], **Patrick T. Norton**[5], and **Jeffrey W. Holmes**[1,6]

[1]Department of Biomedical Engineering, University of Virginia, Charlottesville, VA 22908 USA

[2]Medtronic, Inc., Littleton, MA 01460 USA

[3]Children's Hospital at Dartmouth, Dartmouth-Hitchcock Clinic, Manchester, NH 03104 USA

[4]Billings Clinic, Billings, MT 59107 USA

[5]Department of Radiology, University of Virginia Health System, Charlottesville, VA 22908 USA

[6]Department of Medicine, University of Virginia Health System, Charlottesville, VA 22908 USA

Abstract

Atrial fibrillation is an increasingly prevalent cardiovascular disease; changes in atrial structure and function induced by atrial fibrillation and its treatments are often spatially heterogeneous. However, spatial heterogeneity of function is difficult to assess with standard imaging techniques. This paper describes a method to assess global and regional mechanical function by combining cardiac magnetic resonance imaging and finite-element surface fitting. We used this fitted surface to derive measures of left atrial volume, regional motion, and spatial heterogeneity of motion in 23 subjects, including healthy volunteers and atrial fibrillation patients. We fit the surfaces using a Newton optimization scheme in under 1 min on a standard laptop, with a root mean square error of 2.3±0.5 mm, less than 9% of the mean fitted radius, and an inter-operator variability of less than 10%. Fitted surfaces showed clear definition of the phases of left atrial motion (filling, passive emptying, active contraction) in both volume-time and regional radius-time curves. Averaged surfaces of healthy volunteers and atrial fibrillation patients provided evidence of substantial regional variation in both amount and timing of regional motion, indicating spatial heterogeneity of function, even in healthy adults.

I. Introduction

Atrial fibrillation (AF) is a major source of cardiovascular risk, second only to coronary artery disease [1]. AF is associated with a 4.5-fold increase in stroke risk [2], a decreased quality of life [3], and increased hospitalization costs [4]. Over five million people in the U.S. currently suffer from AF, a number expected to triple by 2050 [5]. Frequent AF episodes damage left atrial (LA) tissue by causing electrical and structural remodeling [6].

Address for Correspondence: Jeffrey Holmes, M.D., Ph.D., F.A.H.A., Professor of Biomedical Engineering and Medicine, Faculty Member, Robert M. Berne Cardiovascular Research Center, University of Virginia, holmes@virginia.edu / http://bme.virginia.edu/holmes/index.html, (434) 243-6321 / (434) 982-3870 fax.

There is increasing evidence that the amount of remodeling varies throughout the atrium [7] [8]. This spatial variation in remodeling creates regional heterogeneity in both structure and function. Electrical heterogeneity is a recognized feature of AF [9], yet structural and mechanical heterogeneity have received less attention [10].

Structural heterogeneity also arises from catheter ablation, which permanently scars atrial tissue. Given the limitations of anti-arrhythmic drugs [11], catheter ablation has become a primary AF therapy [12] [13], and has been proposed as a first-line treatment [14]. Ablation early after diagnosis can prevent recurrence of AF, but does so by adding substantial scar, typically at pulmonary vein ostia and the LA roof. Catheter ablation increases the structural and mechanical heterogeneity of the chamber, with unknown effects on LA contractile function.

Regional heterogeneity of mechanical function could be a valuable indicator in quantifying both disease progression and ablation therapy efficacy. By quantifying regional mechanics, clinicians could potentially: 1) quantify the effects of medical and catheter-based therapies on preserving LA mechanical function, 2) select ablation patterns that minimize injury to regions that contribute most to mechanical function, 3) measure AF-related damage based on loss of mechanical function, and 4) monitor regional function and remodeling following catheter ablation. Measures of atrial mechanical function could also be useful for patients with heart failure, mitral valve disease, or hypertension, all of which are known to adversely affect the left atrium [15] [16] [17]. Methods to quantify atrial function could also be applied to the right atrium, which is ablated in some procedures [18] with unknown effects on right heart mechanical function.

Previous studies have attempted to derive regional mechanics from two dimensional imaging modalities, but conclusions are inconsistent when monitoring post-ablation recovery [19] [20] [21] [22] [23] [24]. Many techniques for measuring regional mechanics, such as echocardiographic speckle tracking, cardiac magnetic resonance (CMR) tagging, and cine displacement encoding stimulated echo (DENSE) CMR, are limited in the atrium by its thin walls, which are typically only 2–3 mm thick. Spacing of CMR tags in human subjects is typically greater than 5 mm [25] [26], while current implementations of 2-D and 3-D DENSE CMR use image resolutions of 2.8 mm [27] [28], neither of which could accurately capture atrial motion. We therefore developed an alternative approach to measuring regional mechanics by fitting data from cine CMR to generate a continuous surface representing the left atrial endocardium in space and time, and quantifying both the amount and timing of its motion.

We generate the endocardial surfaces using the finite element method to divide a continuous body into linked elements connected by nodes, then fit those elements to image-derived data points. This method was first applied to physiological surfaces by [29], who fit an epicardial surface of the left ventricle to data from coronary angiograms. Similar approaches were used to fit the left ventricular endocardium [30] and motion of the ventricle [31]. The approach was extended to fit strain data from MR tagging experiments in [32], [33], [34], and [35], and implanted bead markers in [36]. The method was also used for other physiological structures in [37] and [38]. In any work using surface fitting, common issues arise:

accounting for rigid-body motion, assigning data points to locations on the mesh, scaling nodal parameters across elements, optimizing nodal parameters quickly and accurately, and deriving specific quantitative measures of interest from the fitted surface, all of which are handled differently depending on the structure and application. This paper represents the first application of finite-element fitting and wall motion analysis to quantify 3D regional mechanics in the left atrium. It establishes methods for extracting the required data from clinical CMR images and reducing common sources of inter-observer variability, presents an approach to constructing a coordinate system specifically suited to the atrium, and proposes easily interpreted wall-motion-based measures of regional mechanics. We demonstrate the ability of this approach to generate fitted surface meshes with a mean fitting error of 2.3 mm (less than 10% of the mean surface radius) and inter-operator variability of less than 10%, and to quantify regional heterogeneity of wall motion in healthy volunteers and AF patients.

II. Methods

A. Image Acquisition

All studies were approved by the University of Virginia Institutional Review Board (IRB). Nine healthy volunteers (n=9) and fourteen AF patients (n=14) were recruited from the University of Virginia Health System for a research CMR scan with informed consent. All scans were performed on a 1.5-T Magnetom Avanto (Siemens Healthcare, Erlangen, Germany). A steady-state free procession (SSFP) imaging sequence was employed, with a median flip angle of 71 (range 48, 79) degrees, repetition time of 39 (30, 45) ms, and echo time of 1.4 (1.1, 1.6) ms. Electrocardiographic gating was used in a slice-selective imaging acquisition during held expiration with a 6mm slice thickness. A single slice was acquired in the sagittal and coronal planes, as well as the left vertical long-axis (2 chamber) and horizontal long-axis (4 chamber) planes relative to the heart. A stack of slices was acquired in the axial plane with no interslice gap. Roughly 15–20 axial images were acquired to ensure adequate coverage of the left atrium. The field of view varied depending on the imaging plane, but was approximately 300×300 mm, and the pixel size was 1.2×1.2 mm, where the RF bandwidth was 930 Hz/pixel. Each imaging sequence was reconstructed into 25 time phases, equally spaced across the cardiac cycle based on the R-R interval.

B. Image Processing

CMR images were manually contoured using ARGUS software (Siemens Healthcare). We developed a standardized contouring process in an attempt to reduce inter-operator variability. The left atrium was isolated in the viewing window by centering and magnifying the image. Operators were trained to trace the edge between bright blood and dark surrounding tissue, which best represents the left atrial endocardial surface (Fig. 1a–e). Areas where this edge was absent, specifically the mitral valve orifice, pulmonary vein ostia, and left atrial appendage orifice, required special instruction. Operators were instructed to exclude the left atrial appendage by drawing the contour from the left atrial tissue separating the left pulmonary veins and the left atrial appendage to the intersection of the left atrial appendage and anterior-superior wall (Fig. 1a,d,e). For the mitral valve, operators were instructed to draw contours that crossed the mitral valve annulus into the ventricular cavity

along the direction of neighboring atrial endocardium (Fig. 1c). Contour points below the mitral valve plane were later removed and replaced with a mitral valve "cap" (Sec. II.E). Four pulmonary vein and four mitral valve landmarks were identified at each phase in the cardiac cycle. Three of the four pulmonary veins, including right superior, right inferior, and left inferior, were identified using the stack of axial plane images (Fig. 1a,b,e). The left superior pulmonary vein was identified using the coronal imaging plane (Fig. 1d). Two mitral valve points (lateral and septal) were identified using the horizontal long-axis (4 chamber) plane (Fig. 1f), and two (superior and inferior) were identified using the left vertical long-axis (2 chamber) imaging plane (Fig. 1c).

C. Left Atrial Coordinate System

Contoured and landmarked images were imported into MATLAB r2010b (The MathWorks, Natick, MA, USA), with each contoured pixel treated as a single data point (Fig. 1g). We used the landmarks to create a time-varying coordinate system that accounted for rigid-body motion (Fig. 1h). First, pulmonary vein and mitral valve planes were fit to their respective landmarks. The plane center was defined as the centroid of each landmark group. A vector between the plane centers formed the z-axis of the coordinate system. This axis controlled for tilting of the heart during the cardiac cycle. The pulmonary vein plane required at least 3 landmarks, but could accept more, accommodating variable pulmonary vein anatomy; the left and right pulmonary vein centroids were calculated separately and averaged to find the plane center. A vector from the right pulmonary vein centroid to the left pulmonary vein centroid defined the x-axis, controlling for rotation of the heart. The remaining axis (y) was calculated as the vector cross-product. The bisection of the pulmonary vein-mitral valve axis established the origin of the coordinate system (Fig. 1h, gray arrows) and controlled for translation of the atrium during the cardiac cycle.

D. Finite-Element Mesh

Because the left atrium is roughly spherical, we performed all fitting in spherical coordinates (θ,φ,r). We represented the endocardial surface of the left atrium with a finite-element mesh where the radius varies as a function of space and time, $r=r(\theta,\varphi,r)$. The finite-element mesh is composed of individual elements that intersect at nodes; element coordinates (ξ_1,ξ_2,ξ_t) ranging from 0 to 1 specify the relative location of any point within the element. Polynomial interpolation (basis) functions describe the variation of radius across each element. Following [37], we used cubic Hermite basis functions to interpolate radii in the two spatial dimensions (θ,φ) because the coefficients represent physically meaningful parameters (the radius and its spatial derivative at each node) and because they ensure that the radius and its first derivatives are continuous at all element boundaries (C^1 continuity). We used Lagrange polynomial interpolation in time. The general one-dimensional cubic Hermite interpolation of a variable, y, as a function of position, ξ, in an element is

$$y(\xi)=y_0 H_0^0(\xi)+y_1 H_1^0(\xi)+\left.\frac{\partial y}{\partial \xi}\right|_0 H_0^1(\xi)+\left.\frac{\partial y}{\partial \xi}\right|_1 H_1^1(\xi), \xi \in [0,1], \quad (1)$$

where the nodal values (y_i, $i=\{0,1\}$) and derivatives $(dy/d\xi)_i$ are scaled by four basis functions,

$$H_0^0(\xi)=2\xi^3-3\xi^2+1, H_1^0(\xi)=-2\xi^3+3\xi^2, H_0^1(\xi)=\xi^3-2\xi^2+\xi, H_1^1(\xi)=\xi^3-\xi^2. \quad (2)$$

The general one-dimensional Lagrange interpolation for an m^{th} order polynomial is

$$y(\xi)=\sum_{k=0}^{m} y_k L_k(\xi) \quad (3)$$

where the nodal values (y_k) at positions ξ_k are scaled by m basis functions,

$$L_k(\xi)=\prod_{n=0 n\neq k}^{m} \frac{\xi-\xi_n}{\xi_k-\xi_n}, \xi \in [0,1], k \in \{0,1,\ldots,m\}. \quad (4)$$

We selected element density prior to fitting based on expected variation in the surface through space and time. The spherical surface was divided into 16 elements (4×4), equally spaced in (θ,φ). We chose a seventh-order temporal fit to capture the complex left atrial emptying patterns, requiring eight node locations in the time dimension. Temporal node locations in (4) were spaced at the Chebyshev coefficients, the roots of Chebyshev polynomials described in [39], to add temporal stability and speed of convergence during optimization. Extension of a cubic Hermite interpolation into two dimensions, known as bicubic Hermite, expands (1) to include 4 nodes instead of two, and 4 nodal parameters per node instead of two – nodal values, derivatives in two spatial dimensions, and the cross derivative. An element was created by replicating the 4 bicubic Hermite nodes at 8 temporal locations, creating 32 nodes per element. Each of these 32 nodes contained 4 nodal parameters, creating 128 nodal parameters per element. A complete 16-element mesh, **u**, contained 160 nodes with 640 nodal parameters. Constraints at the poles (Sec. II.G) reduced the total number of independent nodal parameters (degrees of freedom) to 432. We set the initial mesh to a static sphere, with constant radius equal to the median data radius (Fig. 2a).

E. Data Projection

Before projecting data points onto the finite-element mesh, we introduced an artificial mitral valve "cap" to standardize behavior of the fits near the mitral valve orifice (Fig. 1c). Mitral valve annulus points were identified at the intersection between the mitral valve plane and imaging plane contours. Contour points falling beyond the mitral valve plane were removed and replaced with an artificial point set. To ensure a smooth boundary, the position and direction of the left atrial wall immediately adjacent to the annulus were used in a 1-D cubic Hermite function in (1) and (2) to generate the cap. To standardize the impact on the fitted surface, the number of artificial points was scaled to the distance between the annulus points

We projected all data points radially onto the finite-element mesh, allocating points to elements based on their (θ,φ,t) position in spherical space and time (Fig. 2a,b). Following [36], projecting along the fitted dimension provided a single, constant set of element coordinates (ξ_1,ξ_2,ξ_t) for each data point, transforming the complex problem of fitting variations in 4 dimensions (3-D space and time) to the more tractable problem of fitting variations in only the radial dimension (Fig. 2b).

F. Scaling Factors

Mapping data points onto a mesh composed of elements with normalized coordinates ranging from 0 to 1 requires scaling the data, and the effect of that scaling is more complicated when using cubic Hermite basis functions to match both the radius and its derivatives across elements. Consider a one-dimensional function *y(x)* mapped onto one-dimensional elements with element coordinates ξ, so that $y = f(\xi)$ and $\xi = g(x)$. The derivative $\partial y/\partial x$ is defined by the chain rule, where

$$\frac{\partial y}{\partial x}=\frac{\partial y}{\partial \xi}\frac{\partial \xi}{\partial x}. \quad (5)$$

If we choose a linear mapping of x into ξ, scaling between local and global domains will be constant within an element. We can then define a constant scaling factor S as the length of the element, such that $S = \Delta x/\Delta\xi = \Delta x$ if ξ ranges from 0 to 1. This scaling factor is a property of an element and scales the nodal parameters that border it. In order to match the slope between two adjacent one-dimensional elements ($e1$ and $e2$) at the node (n) where they meet, we apply (5) at the node and ensure that

$$\left.\frac{\partial y}{\partial x}\right|_{e1}=\left.\frac{\partial y}{\partial x}\right|_{e2}\rightarrow\left.\frac{\partial y}{\partial \xi}\right|_{n}\left.\frac{\partial \xi}{\partial x}\right|_{e1}=\left.\frac{\partial y}{\partial \xi}\right|_{n}\left.\frac{\partial \xi}{\partial x}\right|_{e2}\rightarrow\left.\frac{\partial y}{\partial \xi}\right|_{n}\frac{1}{S_{e1}}=\left.\frac{\partial y}{\partial \xi}\right|_{n}\frac{1}{S_{e2}}, \quad (6)$$

so that in general if the elements are different sizes and have different scaling factors, matching the physical slope $\partial y/\partial x$ at the joining node requires that the slope in element coordinates $\partial y/\partial\xi$ will not match at the joining node.

For illustration, we sampled a one-dimensional polynomial function *y(x)* and added Gaussian noise to produce a set of *(x,y)* points (Fig. 3a). We then divided the x domain into two elements and projected the sampled data onto those elements. Nodal parameters were optimized to minimize the squared error between the data and the interpolated surface. If elements were evenly spaced, all of the scaling factors were equal and could be disregarded without affecting the fit. However, when we set element spacing to be non-uniform, a normal parametric fit without scaling factors resulted in a slope discontinuity at the element interface (Fig. 3b). Including a scaling factor for each element restored C^1 continuity (Fig. 3c).

In the present work, we scaled each element dimension based on the global space it occupies ($S_\theta=\Delta\theta$, $S_\phi=\Delta\varphi$) and the cross-derivative term by the product of the two scaling factors $S_\theta S_\phi$. The overall interpolation function for an element e becomes

$$\begin{aligned} r(\xi_1,\xi_2,\xi_t)=&r_{ijk}\mathrm{H}_i^0(\xi_1)\mathrm{H}_j^0(\xi_2)\mathrm{L}_k(\xi_t)+\left.\frac{\partial r}{\partial\theta}\right|_{ijk}S_{\theta e}\mathrm{H}_i^1(\xi_1)\mathrm{H}_j^0(\xi_2)\mathrm{L}_k(\xi_t)+\\ &\left.\frac{\partial r}{\partial\phi}\right|_{ijk}S_{\phi e}\mathrm{H}_i^0(\xi_1)\mathrm{H}_j^1(\xi_2)\mathrm{L}_k(\xi_t)+\left.\frac{\partial^2 r}{\partial\theta\partial\phi}\right|_{ijk}S_{\theta e}S_{\phi e}\mathrm{H}_i^1(\xi_1)\mathrm{H}_j^1(\xi_2)\mathrm{L}_k(\xi_t), \end{aligned} \quad (7)$$

where $i = \{0,1\}$, $j = \{0,1\}$, $k = \{0,1,\ldots,m\}$ and summation is implied.

G. Model Constraints

Since we used a spherical surface to represent the atrium, additional constraints were required to ensure continuity at the surface poles (φ=0,π). We constrained nodal radii to be equal and nodal derivatives with respect to the zenith angle (φ) to be the negative of the derivative on the opposite side ($\theta\pm\pi$) of the pole. Partial derivatives with respect to the azimuthal angle (θ) were constrained to be zero, ensuring C^0 and C^1 continuity. Finally, all nodal radii were constrained to be positive. These constraints are summarized as

$$r_k=r_{k+1},\ \left.\frac{\partial r}{\partial \phi}\right|_j=-\left.\frac{\partial r}{\partial \phi}\right|_{j+p/2},\ \left.\frac{\partial r}{\partial \theta}\right|_i=0,\ \left.\frac{\partial^2 r}{\partial\theta\partial\phi}\right|_i=0,\ r_{all\ nodes}>0, \quad (8)$$

where $i = \{0,1,\ldots, p\}$, $j = \{0,1,\ldots,p/2\}$, $k = \{0,1,\ldots,p-1\}$, and p is the number of nodes at the pole of interest.

H. Surface Fitting

We solved the optimization problem using Newton's method to find the nodal parameters that provided the best fit of the model surface to the endocardial data (Fig. 2c). The components of the optimization scheme were: 1) create the error minimization function; 2) impose surface smoothing penalties; 3) ensure necessary parameter constraints; 4) build the objective function; and 5) calculate the necessary gradients and Hessian matrices.

We defined error as the squared difference between the surface radius (r)^and the data point radius ($r_{e,d}$). The surface radius is a function of the data point position ($\xi_{e,d}$) in the element (e) and the nodal parameters and scaling factors (u_e) that define the element. We normalized each element error by the number of points in the element (D_e) to account for variable point density. We computed the total error F as a summation of error across all elements,

$$F=\sum_{e=1}^{E}\frac{1}{D_e}\sum_{d=1}^{D_e}\left\|\hat{r}(u_e,\xi_{e,d})-r_{e,d}\right\|^2. \quad (9)$$

To control surface smoothness, we introduced a Sobolev smoothing constraint, with two constants, α and β, integrated over each element surface (Ω_e) then summed across elements, where

$$G=\sum_{e=1}^{E}\int_{\Omega_e}\left\{\alpha\left\|\frac{\partial\hat{r}}{\partial\xi_1}\right\|^2+\alpha\left\|\frac{\partial\hat{r}}{\partial\xi_2}\right\|^2+\beta\left\|\frac{\partial^2\hat{r}}{\partial{\xi_1}^2}\right\|^2+2\beta\left\|\frac{\partial^2\hat{r}}{\partial\xi_1\partial\xi_2}\right\|^2+\beta\left\|\frac{\partial^2\hat{r}}{\partial{\xi_2}^2}\right\|^2\right\}d\xi_1 d\xi_2 d\xi_t. \quad (10)$$

Here, α represents a penalty on surface stretching and β represents a penalty on surface curvature, as described previously in [36]. Sobolev smoothing factors were set at α=10 and β=1 and integrated using twelve-point Gaussian quadrature. We combined the smoothing function G with the error function, F, to create the objective function. Here, G can be weighted by γ_{Sob} (equivalent to scaling α, β simultaneously) and we typically set γ_{Sob} between 0 and 10^{-2}. Results presented here were obtained with γ_{Sob} set to zero.

Mesh constraints were aggregated into an equation array, **C**. We constructed a Lagrangian, Λ, as the summation of (9), (10) weighted by γ_{Sob}, and the constraints **C** weighted by Lagrange multipliers λ:

$$\Lambda(u,\lambda)=F(u)+\gamma_{Sob}G(u)+\lambda_i C_i. \quad (11)$$

Both the Lagrangian gradient array and Hessian matrix were required for each iteration of the Newton optimization. A solution was achieved when

$$\|\nabla\Lambda(u,\lambda)\|_\infty<\text{Tolerance}. \quad (12)$$

Nonlinear optimization was performed using a sequential quadratic programming algorithm, SQPlab [40] within the MATLAB environment. During an iteration, a quadratic programming subproblem was solved using Newton's method. SQPlab was modified to use the CPLEX Solver (iLOG, Sunnyvale, CA, USA). The convergence tolerance in (12) was set to 1×10^{-10}. Initial Lagrange multipliers were set to equivalent fractional weights, 1/(total number of constraints).

Input data sets contained 20 000 – 85 000 total data points (median size 52 000). A single element typically contained 1500 – 2000 data points. All MATLAB processing was done on either a 3 GHz Intel quad-core processor with 4 GB RAM running Windows XP or 2.4 GHz Intel quad-core (i7) processor with 4 GB RAM running Mac OSX 10.7.

I. Quantitative Wall Motion Analysis

Using the fitted surface, we computed left atrial chamber volume by numerical integration. As a reference, we calculated axial volume by summing the area of axial contours, each scaled by the CMR image slice interval. Volume below the mitral valve plane was discarded. Fractional changes in volume were computed by normalizing chamber volumes to the maximum value for that subject. Fractional changes in radius were assessed using fractional shortening (FS),

$$\text{FS}(\theta,\phi)=\frac{r(\theta,\phi,t_{Vmax})-r(\theta,\phi,t_{Vmin})}{r(\theta,\phi,t_{Vmax})}. \quad (13)$$

To segment the surface into anatomic regions, we used the digitized landmarks (pulmonary veins and mitral valve annulus) to define the posterior wall (the pulmonary valve plane) and mitral valve plane. Between these two planes, we separated the surface into four midwall regions based on 90-degree rotations about the pulmonary vein-mitral valve (z) axis, offset by 45 degrees from the right-to-left pulmonary vein vector. This defined the intra-atrial septum, lateral wall, inferior wall, and superior wall. To create an averaged surface of healthy volunteers or AF patients, we averaged nodal parameters for all the fitted surfaces in the subject group. We then quantified global and regional motion from the averaged surface.

III. Results

A. Image Processing

Inter-observer agreement in slice contour areas and atrial volumes were determined in a two-operator comparison using a subset of CMR data (five AF patients, 3 healthy volunteers). The operators contoured the eight atria at minimum and maximum atrial volumes (ventricular end diastole and end systole, respectively). Operators followed instructions to exclude left atrial appendage and include the MV plane, tracing into the left ventricle (Fig. 4a). The artificial MV cap (dotted line) successfully corrected for variable tracing extensions past the MV plane, producing a similar cap even when the two observer tracings were quite different (Fig. 4a, right). We compared individual contours traced by the two operators using a Bland-Altman analysis of contour areas, including all axial and non-axial imaging planes (Fig. 4b). The average difference in area was 1.4 cm^2 (8.6% of mean slice area), with a 95% CI of ±3.4 cm^2. When atrial volumes were computed as a summation of axial contour area, scaled by the CMR image slice interval, Bland-Altman analysis (Fig. 4c) revealed a small difference in total atrial volumes between operators (5.9 mL, with a 95% CI of ±8.3 mL), which represented 9.0% of the mean volume.

B. Left Atrial Coordinate System

We used anatomic landmarks to create a coordinate system that removed bulk chamber motion. To confirm this, we tracked landmark motion in all N=23 data sets through a single cardiac cycle. The centroid of the pulmonary vein plane translated a small amount during the cardiac cycle (1.8±1.7 mm at peak, mean ± SD; Fig. 5a). The centroid of the mitral valve plane moved much more (11.4±3.0 mm at peak), especially along the PV-MV axis (10.7±2.7 mm at peak; Fig. 5b). Motion of the mitral valve annulus landmarks was not uniform; the inferior MV landmark moved the most (15.8±3.5 mm) and the right MV landmark the least (9.4±3.4 mm), indicating tilting of the mitral valve plane relative to the pulmonary vein centroid. The mitral valve of AF patients moved less than healthy volunteers but the two groups had similar patterns of landmark motion.

C. Surface Fitting

All data sets converged to the specified tolerance of 1×10^{-10} with root mean square error (RMSE) of 2.3±0.5 mm (range 1.4 to 3.4). Fitted regional radii varied between 10 and 42 mm with a mean of 26 mm. The optimization terminated after one iteration and 11±3 seconds computation time. The exact solution had a lower RMSE compared to an alternative quasi-Newton method that did not calculate the Hessian matrix, even when the alternative method was run for over 50 solver iterations. Computation time was dependent on the number of fitted data points and the mesh element density. Sobelov smoothing increased the total computation time but did not affect solver convergence. RMSE did not vary with time in the cardiac cycle ($p=0.99$, one-way ANOVA), or between normal volunteers and AF patients ($p=0.82$, unpaired Student's t-test). We observed the largest errors at (θ,φ) positions where contours from different imaging planes overlapped but disagreed. This disagreement could have arisen from random errors such as contouring error or beat-to-beat variations in left atrial motion, or due to a shift of one slice relative to others induced by variable diaphragm position during held-expiration image acquisition. To assess the potential role of

breath-hold artifacts, we measured the average distance between contours over the cardiac cycle at 569 intersections of 271 contours in the 23 data sets. The average translation was 2.6±2.7 mm. Ten slices (4%) with translation greater than 5 mm were reviewed, but only one was shifted enough to alter computed volumes and fractional shortening; that single slice was omitted from the final analysis.

D. Quantitative Analysis of Left Atrial Volumes

We compared atrial volumes computed by summing axial contours to volumes computed by integrating the fitted 3-D surface. As expected, the two methods generally agreed, and the fitted volumes were smoother in time (Fig. 6a). Fitted volumes matched summed axial volumes in a Bland-Altman analysis (Fig. 6b), with a small positive offset of 7.6±0.2 mL (mean ± std. error). The changes in atrial volume during a normal cardiac cycle were divided into four phases: filling (ventricular systole), passive emptying, diastasis, and active contraction (atrial systole) (Fig. 6a). These four phases were consistently observed in all patient and volunteer atria, but varied in duration and magnitude. Maximum atrial volumes, measured at the end of atrial filling, ranged from 42 to 180 mL, with a mean of 91±29 mL. Fractional change in atrial volume ranged from 34% to 75%, with a mean of 52±11%. Of this total change in volume, 52±16% was active, ranging from 26 to 77% across all volunteer and patient data sets.

E. Quantitative Analysis of Regional Wall Motion

Average regional radius curves for the volunteer atria followed similar patterns of filling and emptying (Fig. 7a) compared to atrial volume (Fig. 6a), and similarly had both passive and active emptying phases. The timing and magnitude of emptying varied substantially among regions. We divided the atrium into six regions and mapped them onto a 2-D Hammer projection [41], displaying the entire left atrial surface (Fig. 7b). Using the continuous fitted surface, we were able to compute radial motion at any point on the left atrial wall. We calculated radial motion and radial fractional shortening (FS) at 6 400 equally spaced points, then projected them onto a 2-D Hammer map, producing a continuous spatial map of left atrial function (Fig. 7c, 7e). The orientation of the Hammer map follows our coordinate system (Fig. 1h), where the z-axis extends from the pulmonary vein plane to the mitral valve plane, or from the North to South pole of the map. The range of regional motion was greatest in the inferior wall (Fig. 7c, 7e, dark blue), and least in the superior wall (light blue). We analyzed regional motion using both a fixed origin at a constant distance from the pulmonary vein center and a floating origin that moved with the mitral valve (Fig. 7c,e and 7d,f, respectively). A fixed origin showed the majority of radial motion and fractional shortening occurred around the mitral valve annulus (Fig. 7c,e). We expected this based on the motion of atrial landmarks around the mitral valve and pulmonary veins (Fig. 5a).

We constructed average wall motion maps for the 9 healthy volunteers and the 14 AF patients. Fractional shortening was depressed in the AF patients (Fig. 8b) compared to the volunteers (Fig. 8a). The regional pattern of motion was consistent between groups, with the highest motion in the lateral and inferior walls and lowest motion in the superior wall. Using local peak detection, the timing of atrial contraction was mapped for each of the 6 400 radial motion points, excluding those where an active contraction peak could not be detected. The

AF patient group had more spatial variation in timing of contraction (Fig. 8d) compared to the more homogeneous volunteer group (Fig. 8c).

IV. Discussion

Atrial fibrillation induces adverse remodeling and fibrosis, which varies regionally. Catheter ablation, a primary treatment for AF, produces atrial scar in specified regions to interrupt aberrant electrical signals. In both disease progression and ablation therapy, the atrium undergoes regional changes that increase spatial heterogeneity of electrical and structural tissue properties. We therefore sought to develop a method to measure regional mechanical function, which could be a valuable indicator in evaluating patient health and procedure efficacy.

Here, we present a method to quantify regional function in the left atrium by tracking heart wall motion. We contoured the endocardial border from a series of CMR images then fitted the contours to a continuous finite element surface mesh and quantified motion throughout the cardiac cycle. Fitted surfaces captured heterogeneous patterns of passive and active emptying while maintaining an RMSE of 2.3±0.5 mm, or 9% of the mean fitted radius. Mechanical function varied across regions of the atrium, in both the healthy and AF hearts. Fitting error did not significantly vary with atrial size, regional motion, or active contraction across N=23 data sets, demonstrating a robust fitting method.

A. Image Processing

Manual contouring is typically a considerable source of variation in medical imaging analysis [42], and we sought to minimize this by standardizing the tracing process. Initial trials revealed that certain regions, including the left atrial appendage, mitral valve annulus, and pulmonary vein ostia, were especially difficult to trace because the operator did not have a clearly identifiable blood-tissue interface. Using standardized instructions and an artificial mitral valve cap, we held operator variation to less than 9% of mean slice area and less than 9% of mean atrial volume. Based on Bland-Altman analysis, we found nine traced images where operator variation exceeded the limits of agreement, and these outliers confirmed our initial suspicions: all nine came from imaging slices that captured the left atrial appendage, pulmonary vein ostia, or the mitral valve. Future versions of the tracing procedure will use feedback from orthogonal imaging planes and a database of traced images to help operators handle these ambiguities.

B. Left Atrial Coordinate System

We designed a time-varying coordinate system to compensate for known whole heart motion. Although the atrium does move relative to the body during a cardiac cycle, the motion is dominated by the piston-like action of the mitral valve while the pulmonary veins remain relatively stationary (Fig. 5). An important component of this coordinate system is the choice of origin, and whether that origin moves with the filling and emptying atrium (Fig. 7). Using a fixed origin emphasized longitudinal spatial heterogeneity (top to bottom in a Hammer map) and masked variations along the midwall (left to right in a Hammer map). Variations between midwall regions were more clearly distinguished using a floating origin.

In the averaged volunteer data set, the floating origin lowered the spatial coefficient of variation (spatial standard deviation normalized to mean motion) for radial motion to 0.38 from 0.84 (Fig. 7c,d) and for fractional shortening to 0.35 from 0.77 (Fig. 7e,f). This decrease of 55% was similar in the averaged AF atrium. We hypothesize that the smaller coefficient of variation in the floating origin approach will provide greater sensitivity for detecting regional abnormalities in atrial wall motion.

C. Surface Fitting

Newton optimization was a departure from the work of [37], who calculated the gradient of the Lagrange function but not the Hessian matrix. We chose to explicitly calculate the Hessian matrix of (11) to improve solver convergence. Since the error function in (9), the smoothing function in (10), and the constraints in (8) were all second order or lower, the Lagrange function was quadratic. Element-based scaling factors did not vary during optimization, thus they did not influence solver iterations. Since the initial and final meshes all had positive nodal radii, optimized surfaces did not contact the inequality constraints in (8). In combination, these factors reduced the optimization to an interior-point problem, ensuring convergence to an exact solution in a single iteration.

D. Left Atrial Volume

Left atrial volume derived from our fitted surface mesh was slightly larger than the traditional CMR volume calculation via the summation of stacked images. Our surface mesh approach incorporates multiple imaging planes beyond the single image stack and utilizes data from the entire cardiac cycle to fit a surface. A Bland-Altman analysis (Fig. 6b) revealed a positive offset of 7.6 mL between the fitted surface volumes and the traditional summed axial stack volumes. Järvinen and colleagues [43] also reported a small positive offset (1.7 mL) between the true volume and CMR volume of cadaveric LA casts. We suspect that the observed offset is generated in the superior and inferior aspects of the atrium, which have poor definition in an axial stack of images, leading to underestimation, but are clearly defined in the coronal and sagittal views and incorporated into surface fits.

Measurements of left atrial volume will be sensitive to the choice in imaging planes. We quantified this sensitivity by removing contour data from an individual imaging plane and refitting a surface. We then measured the deviation between the full and reduced surfaces as a proxy for the sensitivity of the sequestered contour data, and repeated this analysis for every imaging plane in each of the 23 data sets. Omitting a single imaging plane altered computed maximum volumes by ≤1.0 ml on average. The coronal imaging plane was the most valuable, with its loss generating a 1.4±1.4% deviation in maximum atrial volume.

E. Regional Wall Motion

Left atrial surfaces revealed regional heterogeneity of mechanical function, even among healthy volunteers. We observed the greatest wall motion in the inferior wall of healthy volunteers (FS = 39%), of which 71% was passive emptying. In contrast, the superior wall moved the least of the defined walls between the mitral valve and pulmonary veins (FS = 24%), but almost all of that motion was active contraction.

Measurements of regional wall motion may also be sensitive to the choice in imaging planes. We replicated the study described in Section IV.D to analyze the sensitivity of regional motion to omission of individual imaging planes. Omitting a single imaging plane altered computed radial motion by ≤ 0.4 mm on average. Regional motion was the most sensitive to the coronal plane and the superior and medial portions of the axial imaging stack, where removing one plane generated deviations in regional radial motion of 5.4±6.9, 6.1±10.2, and 5.8±11.2%, respectively.

If we assume the atrium is roughly spherical, we can relate regional radial motion to regional wall strain. In a local region of atrial tissue with length s and radius r, change in length of the tissue (Δs) will be proportional to the change in radius (Δr), where $s = r\, d\theta$ and $\Delta s = \Delta r\, d\theta$. Normalization eliminates the $d\theta$ term, so that numerical values of wall strain and radial FS should be equal, $\Delta s/s = \Delta r/r$. Strain has been directly measured by several groups using speckle tracking echocardiography and velocity vector imaging, including [44], [45], [46], and [47]. We compared our results to the average wall strain measured in (n=64) healthy adults in [44] and (n=127) AF patients in [47]. We converted the strain in [44] and [47] to be zero at maximum atrial volume, matching the normalization we used in fractional shortening measurements (Fig. 9a). We estimated the variation of this converted strain based on the coefficient of variation in the strain measurements. The average fractional shortening we reported was in close agreement with average speckle-tracking strains, within 1% in healthy volunteers and 14% in AF patients, both within the standard deviation of the respective groups.

We used a similar approach to compare regional fractional shortening measurements with regional strain data for (n=84) healthy adults reported by Vianna-Pinton and colleagues in [46]. Those investigators used a regional segmentation (5 main regions, 4 mid-wall sections) that was similar to our approach (Fig. 7b), with some differences in nomenclature. Regional strains closely agreed with fractional shortening measures (Fig. 9b), especially in the posterior, inferior, and lateral walls, which all agreed with less than 10% difference. Vianna-Pinton and colleagues [46] also used speckle tracking to catalog the relative timing of atrial contraction based on the time to peak strain rate in each region. We compared these results to the average timing of contraction in volunteers (Fig. 8c) and found very close agreement. Both regional FS and regional strain rate had early contraction in the septal and posterior walls and later contraction in the superior and lateral walls. The total time delay between regional contractions was 2.3% of the R-R interval in our results, compared to 23 msec reported by [46]. If we assume a healthy heart rate of 60–70 beats per minute, this converts to 2.3–2.7% of the R-R interval and agrees with our results.

A continuous surface has the capability to measure motion in passive and active phases, in both in absolute and relative terms. Motion along a single dimension (radial) is a natural outcome of fitting in spherical coordinates and provided a simple measure of motion grounded in a uniform coordinate system. We chose to normalize radial motion to the maximum radius as an analog to ejection fraction and fractional shortening measures in echocardiography. Although fractional volume changes showed lower inter-subject variability than absolute volume changes, normalization did not affect the coefficient of variation of regional measures in this study. We suspect that normalization only corrects for

differences in atrial size, whereas regional motion depends on both the size and shape of a region.

V. Limitations and Future Work

Any measure of left atrial function must provide reliable information in a timely manner to have clinical value. In the proposed method, manual contouring represents the largest limitation in both repeatability and time requirements. We showed that operator error can be held to 9% variation in slice contour size and stacked atrial volume. As stated earlier, future contouring will use semi-automated processing and rely on a reference database of traced images to assist operators and further reduce this error. Semi-automated contouring will also lower the required time (currently 6–8 hours) to manually contour ~400 images. Future work will explore reducing the number of acquired imaging planes to remove redundant images. Proposed methods of automated contouring, including shape-based approaches described in [48] and propagation of contours through time described in [49] and [50] also hold promise for dramatically reducing the time required for segmentation of the endocardial surface.

To quantify AF disease severity, we would like to extend left atrial wall motion analysis to include patients with persistent and permanent AF. Current gating of CMR pulse sequences relies on a consistent R-wave to temporally align imaging slices, so all patients must be in sinus rhythm at the time of scan. Advances in CMR sequence design, including real-time cardiac imaging, may circumvent this problem. In addition, patients could be electrically converted back to sinus rhythm immediately prior to the scan, but severe cases of AF have already failed such therapies. We are unsure of the value in imaging heart wall motion *during* AF, since true mechanical function would be distorted, but quantifying patterns of motion in a fibrillating atrium would be novel.

Choices in mesh design, including element spacing, smoothing constraints, and temporal fitting order, were set heuristically based on existing methods. Once we acquire a larger patient and volunteer database, a complete survey of mesh design could be performed, choosing element schemes and smoothing levels that balance model complexity with variations in atrial shape and motion. Statistical measures, such as information criterion testing, could verify addition of elements and higher order fits as necessary or superfluous, based on the improved quality of the fit compared to the increased degrees-of-freedom.

VI. Conclusions

We introduce here the first application of finite-element fitting and wall motion analysis to quantify 3D regional mechanics in the left atrium. We established methods for extracting the required data from clinical CMR images and reducing common sources of inter-observer variability, presented an approach to constructing a coordinate system specifically suited to the atrium, and proposed easily interpreted wall-motion-based measures of regional mechanics. We demonstrated the ability of this approach to generate fitted surface meshes with a mean fitting error of 2.3 mm (less than 10% of the mean surface radius) and inter-operator variability of less than 10%. Wall motion analysis revealed regional heterogeneity

in atrial function, even in healthy volunteers, and wall motion measures agreed well with recently published speckle-tracking strain measurements. Using this approach, clinicians could assess heterogeneous changes in mechanical function during AF disease progression and following RF ablation treatment. Accurate assessment of an AF disease state and the consequences of proposed interventions could create new treatment benchmarks, refine clinical decisions, and improve long-term outcomes for patients.

Acknowledgment

The authors wish to thank Dr. N. Dasgupta and Dr. D. Lopez for tracing assistance, P. Jensen for discussions regarding nonlinear optimization, and ColorBrewer.org for color maps. This work is supported by a Pre-Doctoral Fellowship (C. Moyer) and an Established Investigator Award (Dr. J. Holmes) from the AHA, and NIH/NHLBI R01 HL-085160 (Dr. J. Holmes).

References

1. Roger VL, Go AS, Lloyd-Jones DM, Adams RJ, Berry JD, Brown TM, Carnethon MR, Dai S, de Simone G, Ford ES, Fox CS, Fullerton HJ, Gillespie C, Greenlund KJ, Hailpern SM, Heit JA, Ho PM, Howard VJ, Kissela BM, Kittner SJ, Lackland DT, Lichtman JH, Lisabeth LD, Makuc DM, Marcus GM, Marelli A, Matchar DB, McDermott MM, Meigs JB, Moy CS, Mozaffarian D, Mussolino ME, Nichol G, Paynter NP, Rosamond WD, Sorlie PD, Stafford RS, Turan TN, Turner MB, Wong ND, Wylie-Rosett J, on behalf of the American Heart Association Statistics Committee and Stroke Statistics Subcommittee. Roger VL, Turner MB. On behalf of the American Heart Association Heart Disease and Stroke Statistics Writing Group. Heart Disease and Stroke Statistics--2011 Update: A Report From the American Heart Association. Circulation. 2011 Feb. 123(4):e18–e209. [PubMed: 21160056]
2. Wolf P, Abbott R, Kannel W. Atrial fibrillation as an independent risk factor for stroke: the Framingham Study. Stroke. 1991 Aug.22(8):983–988. [PubMed: 1866765]
3. Dorian P, Jung W, Newman D, Paquette M, Wood K, Ayers GM, Camm J, Akhtar M, Luderitz B. The impairment of health-related quality of life in patients with intermittent atrial fibrillation: implications for the assessment of investigational therapy. J Am Coll Cardiol. 2000 Oct.36(4): 1303–1309. [PubMed: 11028487]
4. Wolf PA, Mitchell JB, Baker CS, Kannel WB, D'Agostino RB. Impact of Atrial Fibrillation on Mortality, Stroke, and Medical Costs. Arch Intern Med. 1998 Feb.158(3):229–234. [PubMed: 9472202]
5. Miyasaka Y, Barnes ME, Gersh BJ, Cha SS, Bailey KR, Abhayaratna WP, Seward JB, Tsang TSM. Secular Trends in Incidence of Atrial Fibrillation in Olmsted County, Minnesota, 1980 to 2000, and Implications on the Projections for Future Prevalence. Circulation. 2006 Jul.114(2):119–125. [PubMed: 16818816]
6. Allessie M, Ausma J, Schotten U. Electrical, contractile and structural remodeling during atrial fibrillation. Cardiovasc Res. 2002 May; 54(2):230–246. [PubMed: 12062329]
7. Oakes RS, Badger TJ, Kholmovski EG, Akoum N, Burgon NS, Fish EN, Blauer JJE, Rao SN, DiBella EVR, Segerson NM, Daccarett M, Windfelder J, McGann CJ, Parker D, MacLeod RS, Marrouche NF. Detection and quantification of left atrial structural remodeling with delayed-enhancement magnetic resonance imaging in patients with atrial fibrillation. Circulation. 2009 Apr. 119(13):1758–1767. [PubMed: 19307477]
8. Platonov PG, Mitrofanova LB, Orshanskaya V, Ho SY. Structural Abnormalities in Atrial Walls Are Associated With Presence and Persistency of Atrial Fibrillation But Not With Age. J Am Coll Cardiol. 2011 Nov.58(21):2225–2232. [PubMed: 22078429]
9. Fareh S, Villemaire C, Nattel S. Importance of Refractoriness Heterogeneity in the Enhanced Vulnerability to Atrial Fibrillation Induction Caused by Tachycardia-Induced Atrial Electrical Remodeling. Circulation. 1998 Nov.98(20):2202–2209. [PubMed: 9815876]
10. Corradi D, Callegari S, Maestri R, Benussi S, Alfieri O. Structural remodeling in atrial fibrillation. Nat Clin Pract Cardiovasc Med. 2008 Oct.5(12):782–796. [PubMed: 18852714]

11. Van Gelder IC, Hagens VE, Bosker HA, Kingma JH, Kamp O, Kingma T, Said SA, Darmanata JI, Timmermans AJM, Tijssen JGP, Crijns HJGM. A comparison of rate control and rhythm control in patients with recurrent persistent atrial fibrillation. N. Engl. J. Med. 2002 Dec.347(23):1834–1840. [PubMed: 12466507]
12. Wann LS, Curtis AB, January CT, Ellenbogen KA, Lowe JE, Estes NAM, Page RL, Ezekowitz MD, Slotwiner DJ, Jackman WM, Stevenson WG, Tracy CM, Jacobs AK. 2011 Writing Group Members. 2011 ACCF/AHA/HRS Focused Update on the Management of Patients With Atrial Fibrillation (Updating the 2006 Guideline): A Report of the American College of Cardiology Foundation/American Heart Association Task Force on Practice Guidelines. Circulation. 2011 Jan. 123(1):104–123. [PubMed: 21173346]
13. Pappone C, Augello G, Sala S, Gugliotta F, Vicedomini G, Gulletta S, Paglino G, Mazzone P, Sora N, Greiss I, Santagostino A, LiVolsi L, Pappone N, Radinovic A, Manguso F, Santinelli V. A Randomized Trial of Circumferential Pulmonary Vein Ablation Versus Antiarrhythmic Drug Therapy in Paroxysmal Atrial Fibrillation: The APAF Study. Journal of the American College of Cardiology. 2006 Dec.48(11):2340–2347. [PubMed: 17161267]
14. Wazni OM, Marrouche NF, Martin DO, Verma A, Bhargava M, Saliba W, Bash D, Schweikert R, Brachmann J, Gunther J, Gutleben K, Pisano E, Potenza D, Fanelli R, Raviele A, Themistoclakis S, Rossillo A, Bonso A, Natale A. Radiofrequency Ablation vs Antiarrhythmic Drugs as First-line Treatment of Symptomatic Atrial Fibrillation. JAMA: The Journal of the American Medical Association. 2005 Jun.293(21):2634–2640.
15. Rossi A, Cicoira M, Florea VG, Golia G, Florea ND, Khan AA, Murray STM, Nguyen JT, O'Callaghan P, Anand IS, Coats A, Zardini P, Vassanelli C, Henein M. Chronic heart failure with preserved left ventricular ejection fraction: Diagnostic and prognostic value of left atrial size. International Journal of Cardiology. 2006 Jun.110(3):386–392. [PubMed: 16325283]
16. Verheule S, Wilson E, Everett T, Shanbhag S, Golden C, Olgin J. Alterations in Atrial Electrophysiology and Tissue Structure in a Canine Model of Chronic Atrial Dilatation Due to Mitral Regurgitation. Circulation. 2003 May; 107(20):2615–2622. [PubMed: 12732604]
17. Vaziri SM, Larson MG, Lauer MS, Benjamin EJ, Levy D. Influence of Blood Pressure on Left Atrial Size The Framingham Heart Study. Hypertension. 1995 Jun.25(6):1155–1160. [PubMed: 7768556]
18. Haíssaguerre M, Jaís P, Shah DC, Gencel L, Pradeau V, Garrigues S, Chouairi S, Hocini M, Le Métayer P, Roudaut R, Clémenty J. Right and Left Atrial Radiofrequency Catheter Therapy of Paroxysmal Atrial Fibrillation. Journal of Cardiovascular Electrophysiology. 1996; 7(12):1132–1144. [PubMed: 8985802]
19. Nori D, Raff G, Gupta V, Gentry R, Boura J, Haines DE. Cardiac magnetic resonance imaging assessment of regional and global left atrial function before and after catheter ablation for atrial fibrillation. J Interv Card Electrophysiol. 2009 Nov.26(2):109–117. [PubMed: 19629666]
20. Perea RJ, Tamborero D, Mont L, De Caralt TM, Ortiz JT, Berruezo A, Matiello M, Sitges M, Vidal B, Sanchez M, Brugada J. Left Atrial Contractility is Preserved After Successful Circumferential Pulmonary Vein Ablation in Patients with Atrial Fibrillation. J Cardiovasc Electrophysiol. 2008 Apr.19(4):374–379. [PubMed: 18266672]
21. Wylie JV, Peters DC, Essebag V, Manning WJ, Josephson ME, Hauser TH. Left atrial function and scar after catheter ablation of atrial fibrillation. Heart Rhythm. 2008 May; 5(5):656–662. [PubMed: 18452866]
22. Thomas L, Boyd A, Thomas SP, Schiller NB, Ross DL. Atrial structural remodelling and restoration of atrial contraction after linear ablation for atrial fibrillation. Eur. Heart J. 2003 Nov. 24(21):1942–1951. [PubMed: 14585253]
23. Verma A, Kilicaslan F, Adams JR, Hao S, Beheiry S, Minor S, Ozduran V, Claude Elayi S, Martin DO, Schweikert RA, Saliba W, Thomas JD, Garcia M, Klein A, Natale A. Extensive ablation during pulmonary vein antrum isolation has no adverse impact on left atrial function: an echocardiography and cine computed tomography analysis. J. Cardiovasc. Electrophysiol. 2006 Jul.17(7):741–746. [PubMed: 16836670]
24. Lemola K, Desjardins B, Sneider M, Case I, Chugh A, Good E, Han J, Tamirisa K, Tsemo A, Reich S, Tschopp D, Igic P, Elmouchi D, Bogun F, Pelosi F Jr, Kazerooni E, Morady F, Oral H.

Effect of left atrial circumferential ablation for atrial fibrillation on left atrial transport function. Heart Rhythm. 2005 Sep.2(9):923–928. [PubMed: 16171744]

25. O'Dell WC, Moore CC, Hunter WC, Zerhouni EA, McVeigh ER. Three-dimensional Myocardial Deformations: Calculation with Displacement Field Fitting to Tagged MR Images1. Radiology. 1995 Jun.195(3):829–835. [PubMed: 7754016]
26. Liu W, Ashford MW, Chen J, Watkins MP, Williams TA, Wickline SA, Yu X. MR tagging demonstrates quantitative differences in regional ventricular wall motion in mice, rats, and men. Am J Physiol Heart Circ Physiol. 2006 Nov.291(5):H2515–H2521. [PubMed: 16751290]
27. Spottiswoode BS, Zhong X, Hess AT, Kramer CM, Meintjes EM, Mayosi BM, Epstein FH. Tracking myocardial motion from cine DENSE images using spatiotemporal phase unwrapping and temporal fitting. IEEE Trans Med Imaging. 2007 Jan.26(1):15–30. [PubMed: 17243581]
28. Zhong X, Spottiswoode BS, Meyer CH, Kramer CM, Epstein FH. Imaging three-dimensional myocardial mechanics using navigator-gated volumetric spiral cine DENSE MRI. Magn Reson Med. 2010 Jun.
29. Young A, Hunter P, Smaill B. Epicardial surface estimation from coronary angiograms. Computer Vision, Graphics, and Image Processing. 1989 Jul.47(1):111–127.
30. Nielsen PM, Grice IJL, Smaill BH, Hunter PJ. Mathematical model of geometry and fibrous structure of the heart. Am J Physiol Heart Circ Physiol. 1991 Apr.260(4):H1365–H1378.
31. Young AA, Hunter PJ, Smaill BH. Estimation of epicardial strain using the motions of coronary bifurcations in biplane cineangiography. IEEE Transactions on Biomedical Engineering. 1992 May; 39(5):526–531. [PubMed: 1526643]
32. Young AA, Kramer CM, Ferrari VA, Axel L, Reichek N. Three-dimensional left ventricular deformation in hypertrophic cardiomyopathy. Circulation. 1994 Aug.90(2):854–867. [PubMed: 8044957]
33. Young AA, Kraitchman DL, Dougherty L, Axel L. Tracking and finite element analysis of stripe deformation in magnetic resonance tagging. IEEE Transactions on Medical Imaging. 1995 Sep. 14(3):413–421. [PubMed: 18215845]
34. Young AA, Fayad ZA, Axel L. Right ventricular midwall surface motion and deformation using magnetic resonance tagging. Am J Physiol Heart Circ Physiol. 1996 Dec.271(6):H2677–H2688.
35. Young AA. Model tags: direct three-dimensional tracking of heart wall motion from tagged magnetic resonance images. Medical Image Analysis. 1999 Dec.3(4):361–372. [PubMed: 10709701]
36. Hashima AR, Young AA, McCulloch AD, Waldman LK. Nonhomogeneous analysis of epicardial strain distributions during acute myocardial ischemia in the dog. Journal of Biomechanics. 1993 Jan.26(1):19–35. [PubMed: 8423166]
37. Bradley CP, Pullan AJ, Hunter PJ. Geometric modeling of the human torso using cubic hermite elements. Ann Biomed Eng. 1997 Feb.25(1):96–111. [PubMed: 9124743]
38. Smith DB, Sacks MS, Vorp DA, Thornton M. Surface Geometric Analysis of Anatomic Structures Using Biquintic Finite Element Interpolation. Annals of Biomedical Engineering. 2000 Jun.28(6): 598–611. [PubMed: 10983706]
39. Mason, JC.; Handscomb, DC. Chebyshev polynomials. CRC Press; 2003.
40. Bonnans, JJF.; Gilbert, JC.; Lemaréchal, C. Numerical Optimization. Springer; 2007.
41. Yang, QH.; Snyder, JP.; Tobler, WR. Map Projection Transformation: Principles and Applications. CRC Press; 2000.
42. Danilouchkine MG, Westenberg JJM, de Roos A, Reiber JHC, Lelieveldt BPF. Operator induced variability in cardiovascular MR: left ventricular measurements and their reproducibility. J Cardiovasc Magn Reson. 2005; 7(2):447–457. [PubMed: 15881528]
43. Järvinen V, Kupari M, Hekali P, Poutanen V-P. Assessment of left atrial volumes and phasic function using cine magnetic resonance imaging in normal subjects. The American Journal of Cardiology. 1994 Jun.73(15):1135–1138. [PubMed: 8198044]
44. Saraiva RM, Demirkol S, Buakhamsri A, Greenberg N, Popovic ZB, Thomas JD, Klein AL. Left Atrial Strain Measured by Two-Dimensional Speckle Tracking Represents a New Tool to Evaluate Left Atrial Function. Journal of the American Society of Echocardiography. 2010 Feb.23(2):172–180. [PubMed: 20152699]

45. Kuppahally SS, Akoum N, Burgon NS, Badger TJ, Kholmovski EG, Vijayakumar S, Rao SN, Blauer J, Fish EN, DiBella EVR, MacLeod RS, McGann C, Litwin SE, Marrouche NF. Left Atrial Strain and Strain Rate in Patients With Paroxysmal and Persistent Atrial Fibrillation: Relationship to Left Atrial Structural Remodeling Detected by Delayed-Enhancement MRI. Circ Cardiovasc Imaging. 2010 May; 3(3):231–239. [PubMed: 20133512]

46. Vianna-Pinton R, Moreno CA, Baxter CM, Lee KS, Tsang TSM, Appleton CP. Two-dimensional speckle-tracking echocardiography of the left atrium: feasibility and regional contraction and relaxation differences in normal subjects. J Am Soc Echocardiogr. 2009 Mar.22(3):299–305. [PubMed: 19258177]

47. Motoki H, Dahiya A, Bhargava M, Wazni OM, Saliba WI, Marwick TH, Klein AL. Assessment of Left Atrial Mechanics in Patients with Atrial Fibrillation: Comparison between Two-Dimensional Speckle-Based Strain and Velocity Vector Imaging. Journal of the American Society of Echocardiography. 2012 Apr.25(4):428–435. [PubMed: 22265458]

48. Tsai A, Yezzi J, Wells AW, Tempany C, Tucker D, Fan A, Grimson WE, Willsky A. A shape-based approach to the segmentation of medical imagery using level sets. IEEE Transactions on Medical Imaging. 2003; 22(2):137–154. [PubMed: 12715991]

49. Jolly M-P. Automatic Segmentation of the Left Ventricle in Cardiac MR and CT Images. International Journal of Computer Vision. 2006 Nov.70(2):151–163.

50. Lynch M, Ghita O, Whelan PF. Segmentation of the Left Ventricle of the Heart in 3-D+t MRI Data Using an Optimized Nonrigid Temporal Model. IEEE Transactions on Medical Imaging. 2008; 27(2):195–203. [PubMed: 18334441]

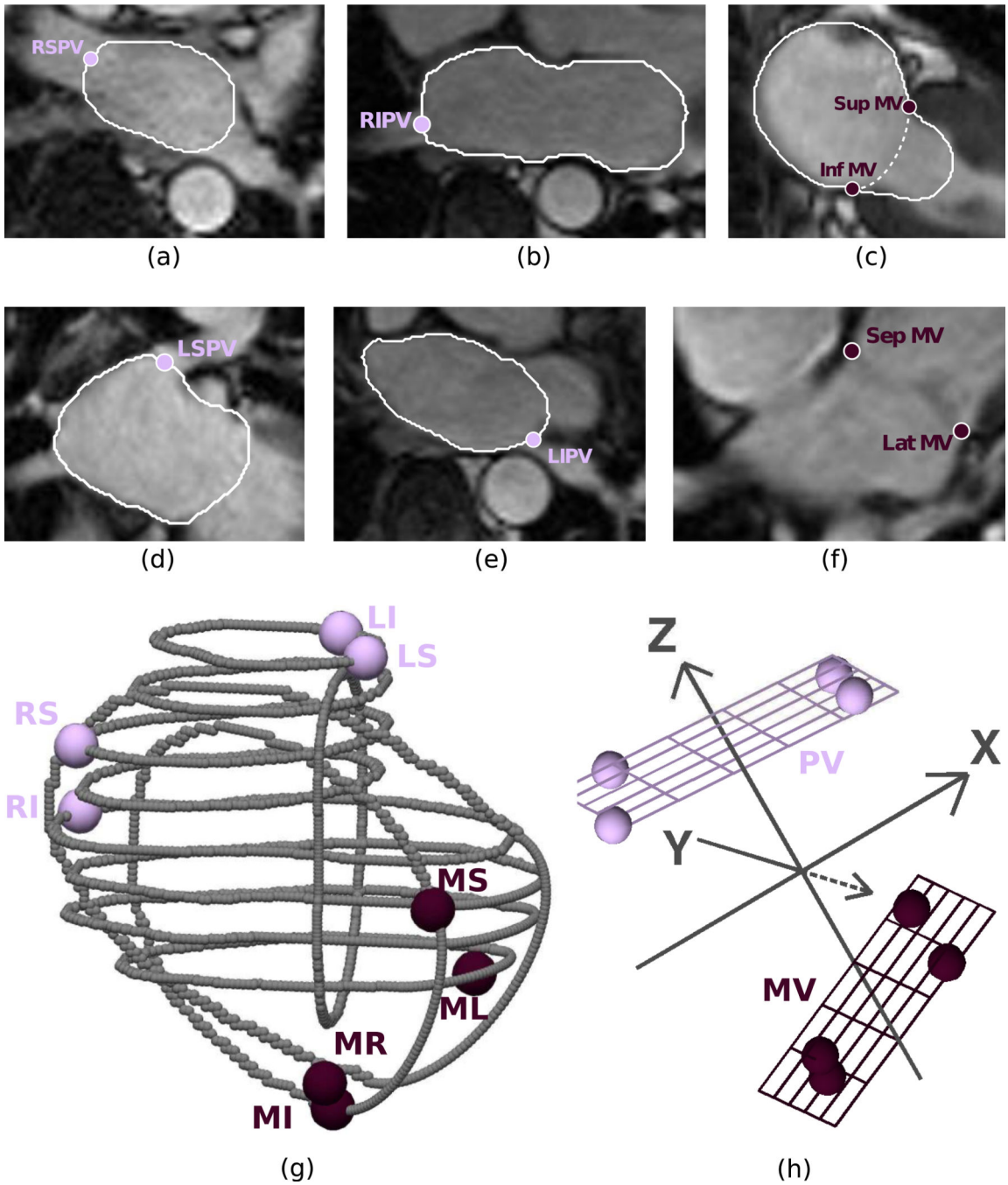

Figure 1.

Contouring, landmarking, and orienting the atrium. (a–e) The left atrial endocardial border is traced in cine CMR images, handling abnormal regions by cropping the left atrial appendage in (a,d,e) and tracing through the mitral valve plane in (c). Contours below the mitral valve plane are removed and replaced with an artificial “cap” (dotted line). Landmarks are identified for the four pulmonary veins (light circles) and the mitral valve annulus (dark circles). (a,b,e) Axial images are used to find the right superior, right inferior, and left inferior pulmonary veins (RSPV, RIPV, LIPV). (d) The coronal view is used to find the left

superior pulmonary vein (LSPV). (c) The 2-chamber view is used to find the superior (Sup, MS) and inferior (Inf, MI) mitral valve (MV) landmarks. (f) The 4-chamber view is used to find the septal/right (Sep, MR) and lateral/left (Lat, ML) mitral valve landmarks. (g) Contours are converted to a four-dimensional point cloud (gray points), along with four pulmonary vein landmarks (light) and four mitral valve landmarks (dark), labeled accordingly. (h) Landmarks form the basis for a time-varying coordinate system. Pulmonary vein and mitral valve landmarks are fit to planes (hatched), and the respective landmark centroids form the z-axis (gray arrow). The right-to-left pulmonary vein vector defines the x-axis. A vector cross-product defines the y-axis. The coordinate system origin (intersection of gray arrows) is defined by the bisection of the pulmonary vein and mitral valve landmark centroids.

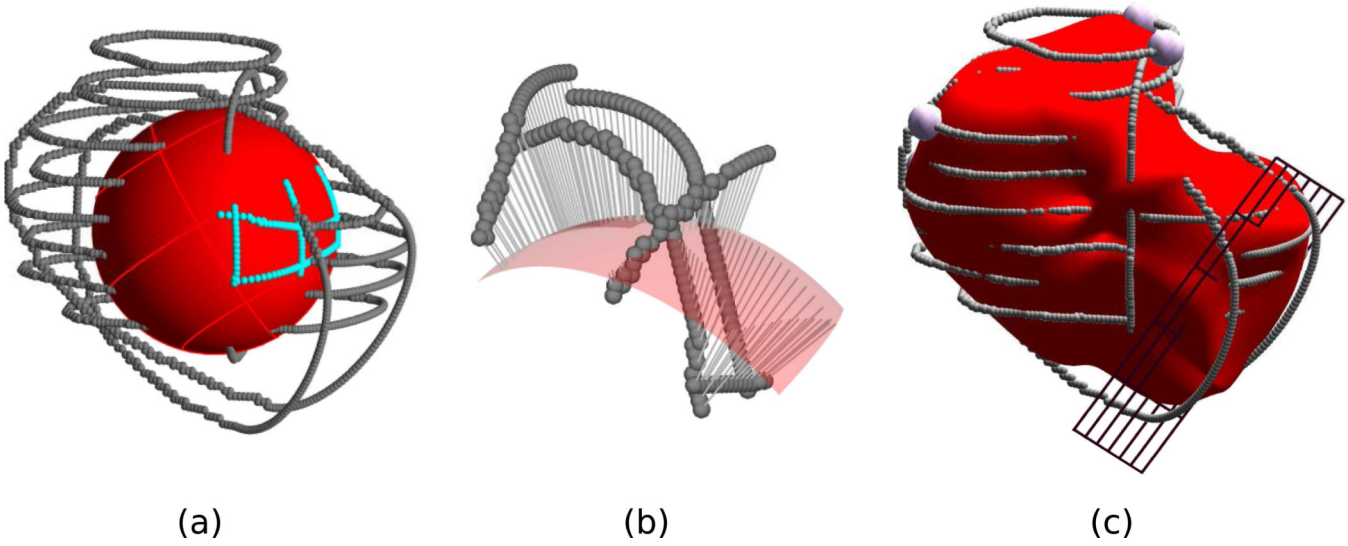

Figure 2.

Mesh generation, projection, and optimization. (a) A 16-element static spherical mesh (red) is generated in the transformed coordinate system. Elements (red lines) are equally spaced in spherical coordinates (θ,φ). Contour points are assigned to an element (cyan points) based on their spherical position and (b) projected along the fitted dimension (radius) onto the surface (gray lines). (c) Mesh parameters are optimized to minimize the error between contour point radii (gray points) and projected mesh radii (red surface), producing a continuous surface in space and time.

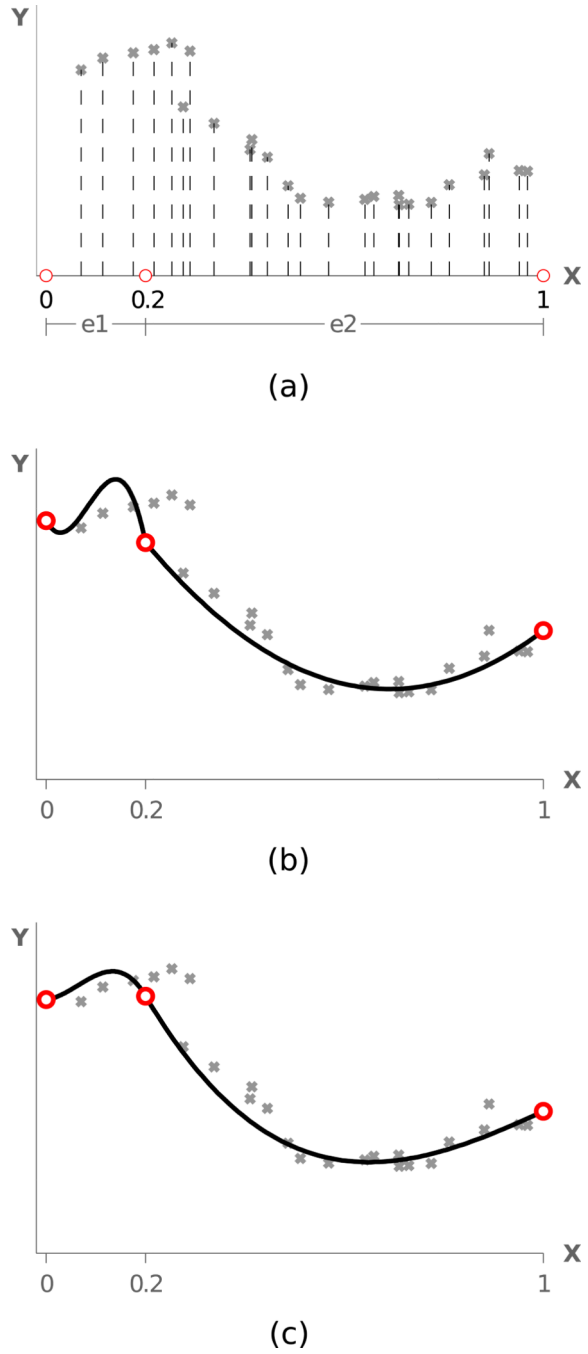

Figure 3.

Scaling factors in a 1-D fit. (a) Noisy data (gray x's) are allocated into two elements (e1,e2), bounded by nodes (red circles), then fit to a 1-D function using Newton optimization. (b) Cubic Hermite interpolation relies on nodal values and derivatives; matching element slope at each node creates a discontinuity in physical slope in a 1-D fit (black line) when adjacent elements are different sizes. (c) Scaling factors account for the unequal element size and correct the fit, resulting in a smooth function.

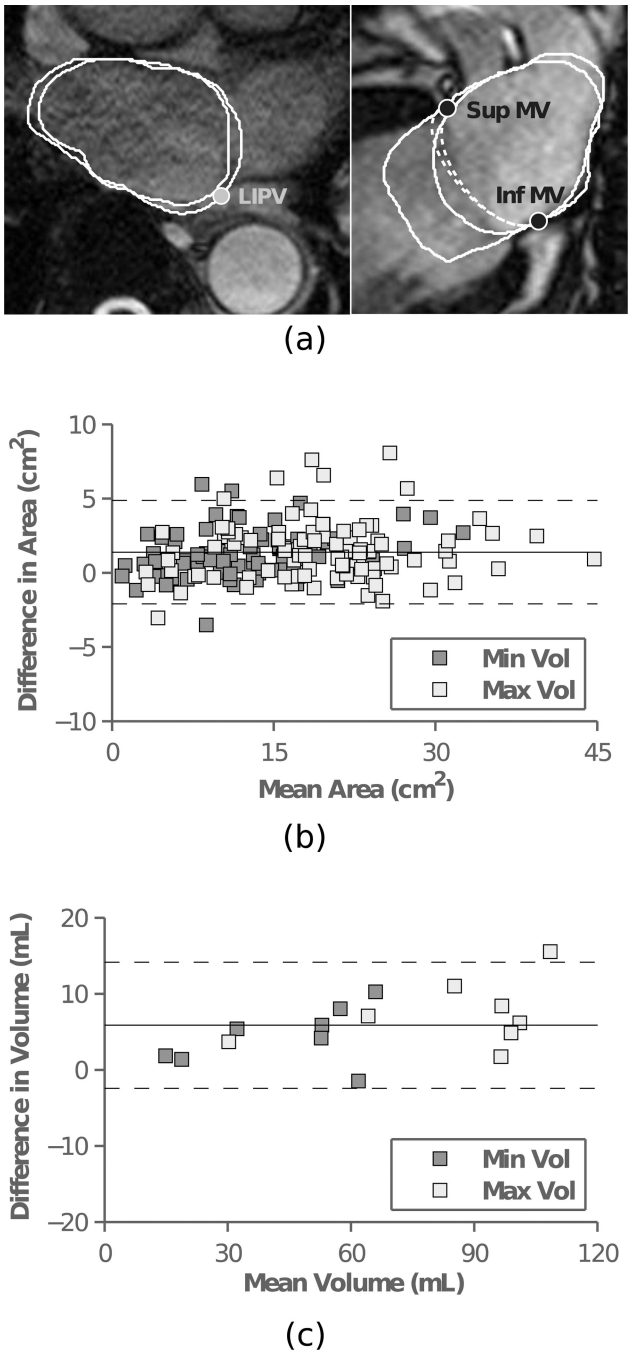

Figure 4.

Inter-operator variability in contouring. (a) Traces of two operators (solid white lines) follow standards of removing left atrial appendage (left panel) and tracing through the mitral valve plane (right panel). The mitral valve cap (dotted lines) successfully standardizes contours below the mitral valve plane. (b) Eight atria were traced by two operators at the minimum and maximum atrial volumes, then compared based on contour area using Bland-Altman analysis. (c) Bland-Altman analysis of atrial volumes, based on summation of axial contour

areas. Solid line represents mean difference, and dotted lines represent 95% confidence interval about that mean.

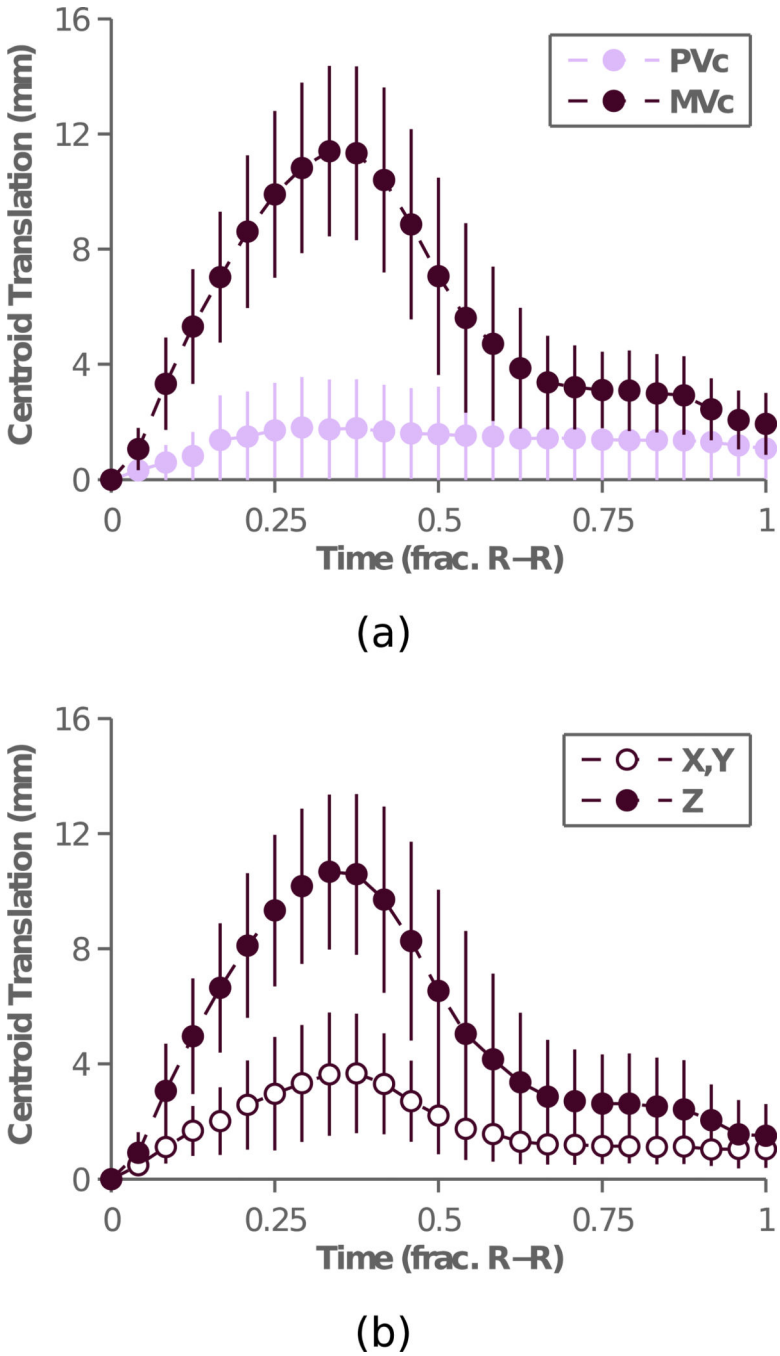

Figure 5.

Landmark motion during the cardiac cycle. Mitral valve (MV) and pulmonary vein (PV) landmarks create a time-varying coordinate system that compensates for bulk motion and rotation. Error bars represent mean±SD. (a) The MV annulus plane center (MVc, dark circles) translates over 10mm during atrial filling. The PV plane center (PVc, light circles) shifts slightly during filling and emptying. (b) The majority of MVc motion occurs along the z-axis (filled circles), but there is substantial motion in the x-y plane (open circles) due to the tilting of the mitral valve relative to the pulmonary veins.

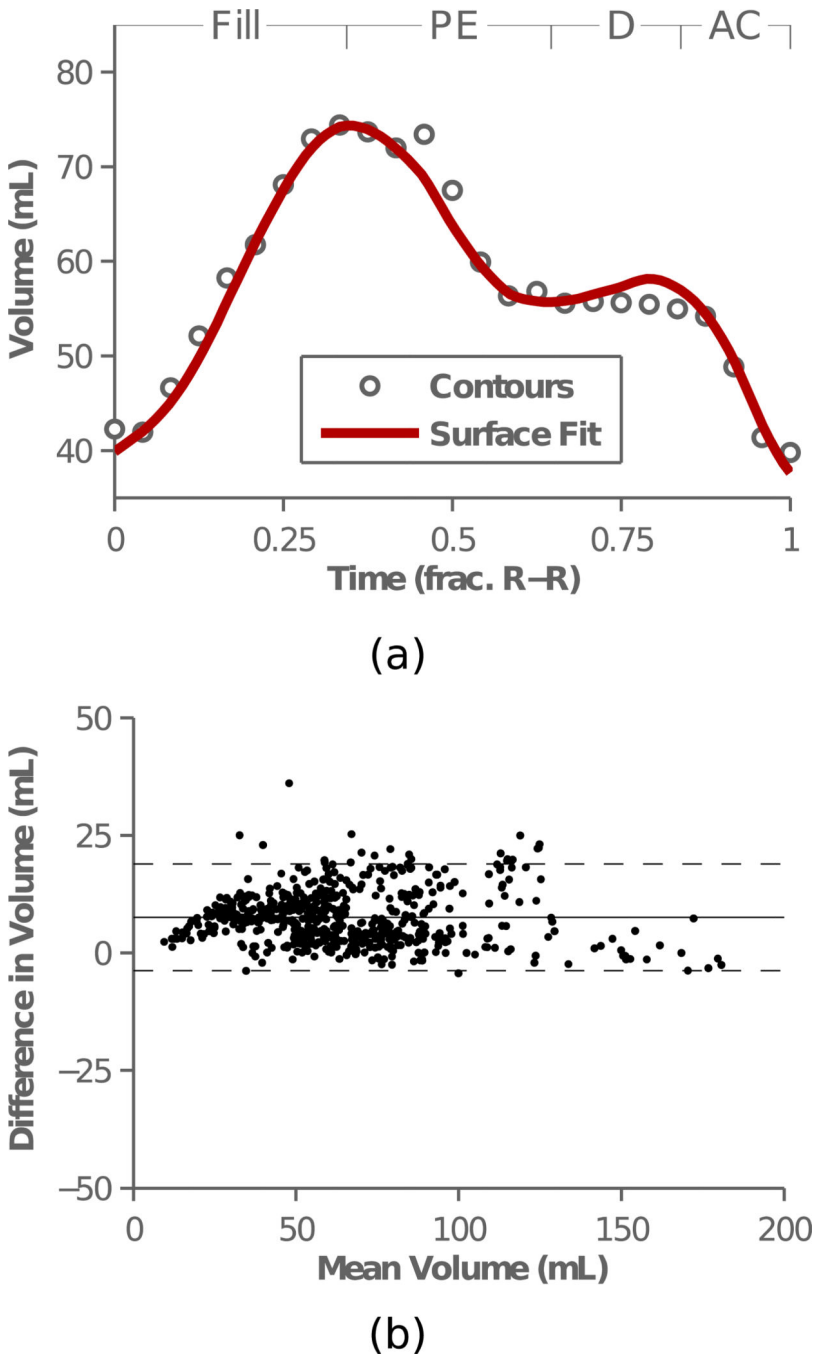

Figure 6.

Quantitative analysis of left atrial volumes. (a) The volume curve (red) of a fitted left atrial surface through a complete cardiac cycle (R-wave to R-wave). Fitted volumes matched summed axial contour volumes (gray circles) well. Volume curves can be divided into four phases: filling, passive emptying (PE), diastasis (D), and active contraction (AC). (b) A Bland-Altman plot comparing surface fit volumes to summed axial volumes. Surface volumes matched summed axial volumes for N=23 data sets, with a small but consistent positive offset.

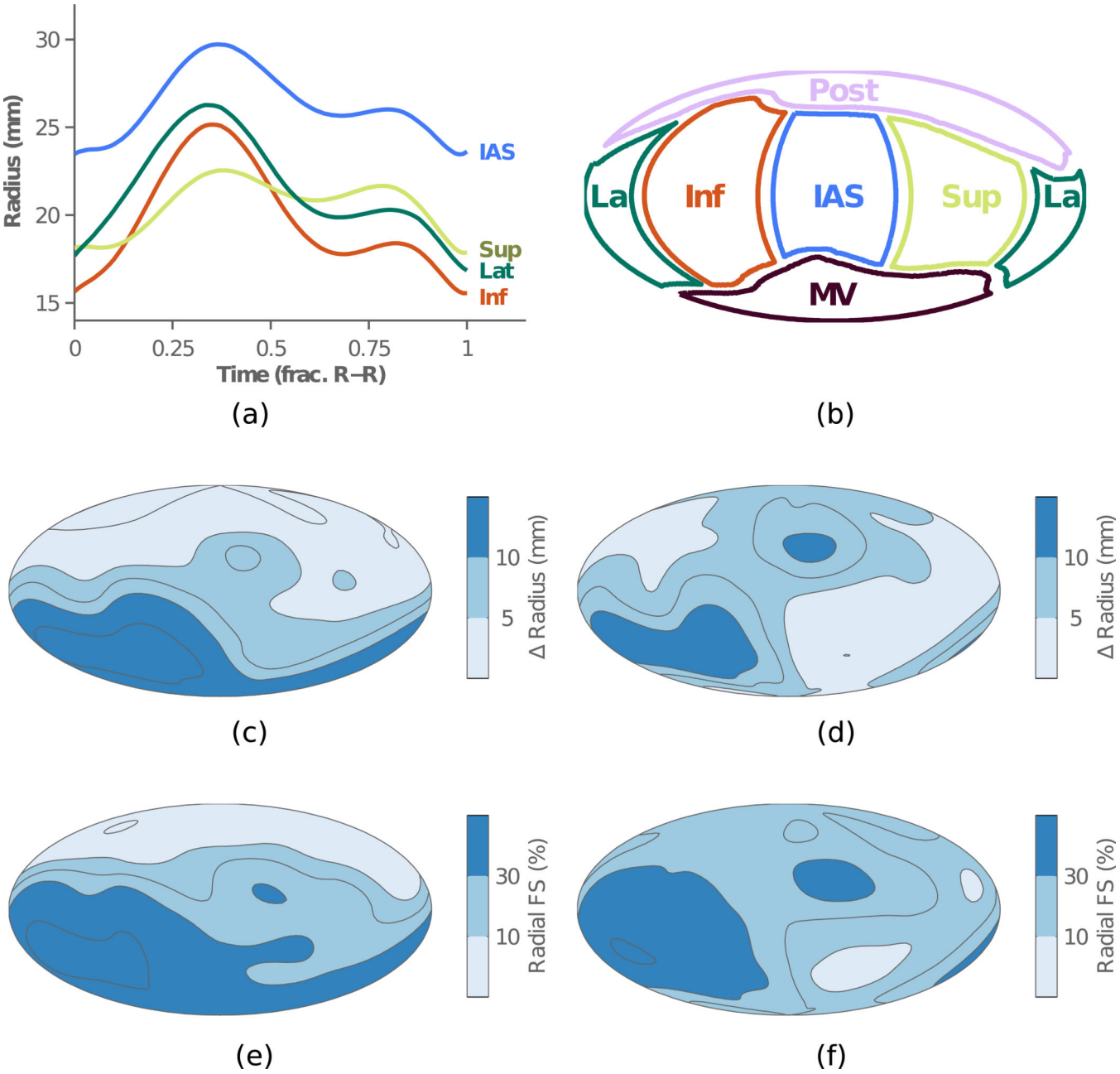

Figure 7.

Regional function and impact of origin definition. (a) Regional radius vs. time curves for an averaged volunteer atrium, using a fixed coordinate origin. Regional motion follows volumetric patterns of filling and emptying, but varies in timing and extent of motion. The atrium is divided into four midwall regions: the intra-atrial septum (IAS), superior wall (Sup), lateral wall (Lat), and the inferior wall (Inf). (b) Surface regions can be mapped onto a 2-D Hammer projection, oriented along the posterior wall (Post) – mitral valve (MV) axis. (c–f) Measures of mechanical function, such as (c,d) radial motion and (e,f) fractional shortening, can be mapped similarly. Darker blue indicates greater regional function. Regional analysis identified the greatest range of regional motion in the inferior and lateral

walls. Longitudinal variations were more apparent when using a fixed origin (c,e), while using a floating origin (d,f) emphasized variation around the midwall.

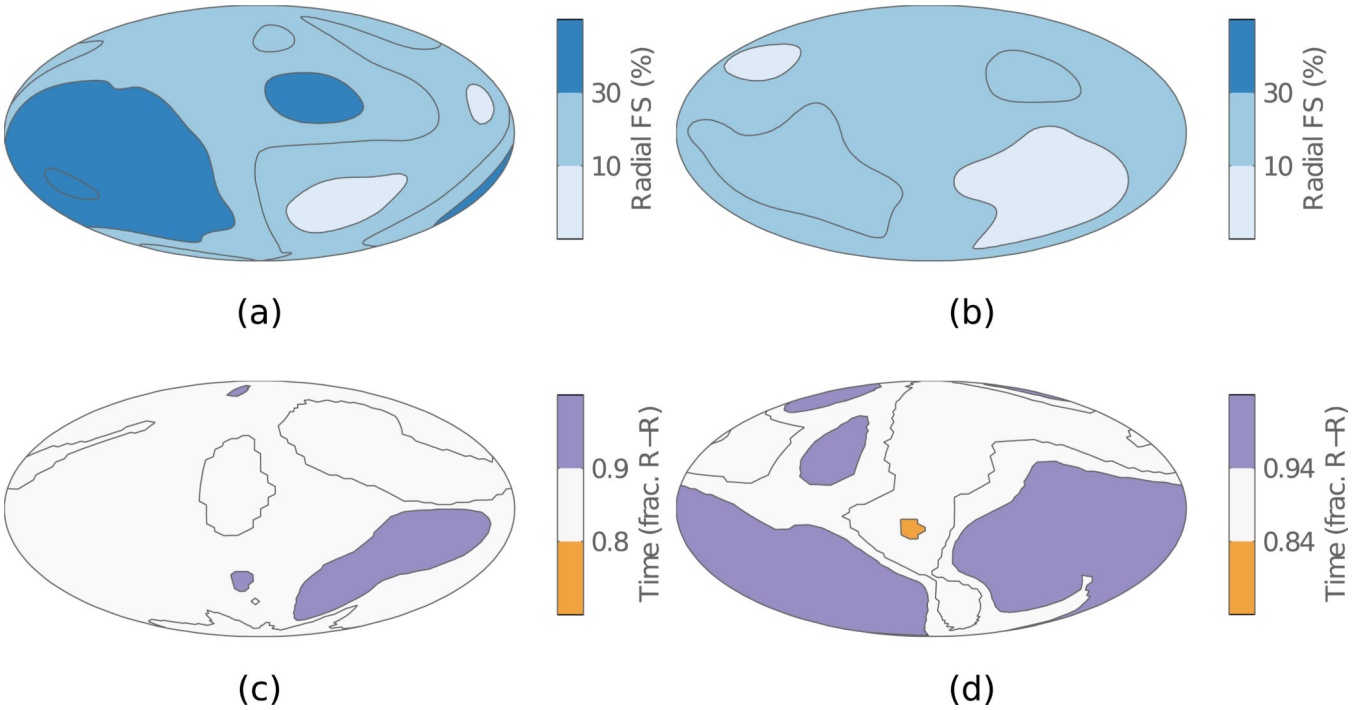

Figure 8.

Comparison of average regional function in volunteer and AF patient groups. (a,b) Fractional shortening was higher in the healthy volunteers (a) and lower in the AF patients (b). The atrium moves more in the inferior and lateral walls compared to the superior wall in both cases. Darker blue represents greater regional function. (c,d) Regional timing of contraction, based on local peaks of the radius vs. time curves, becomes more variable in the averaged AF patient surface (d) compared to the healthy volunteer (c). Orange and purple areas represent regions that contracted earlier and later than average, respectively.

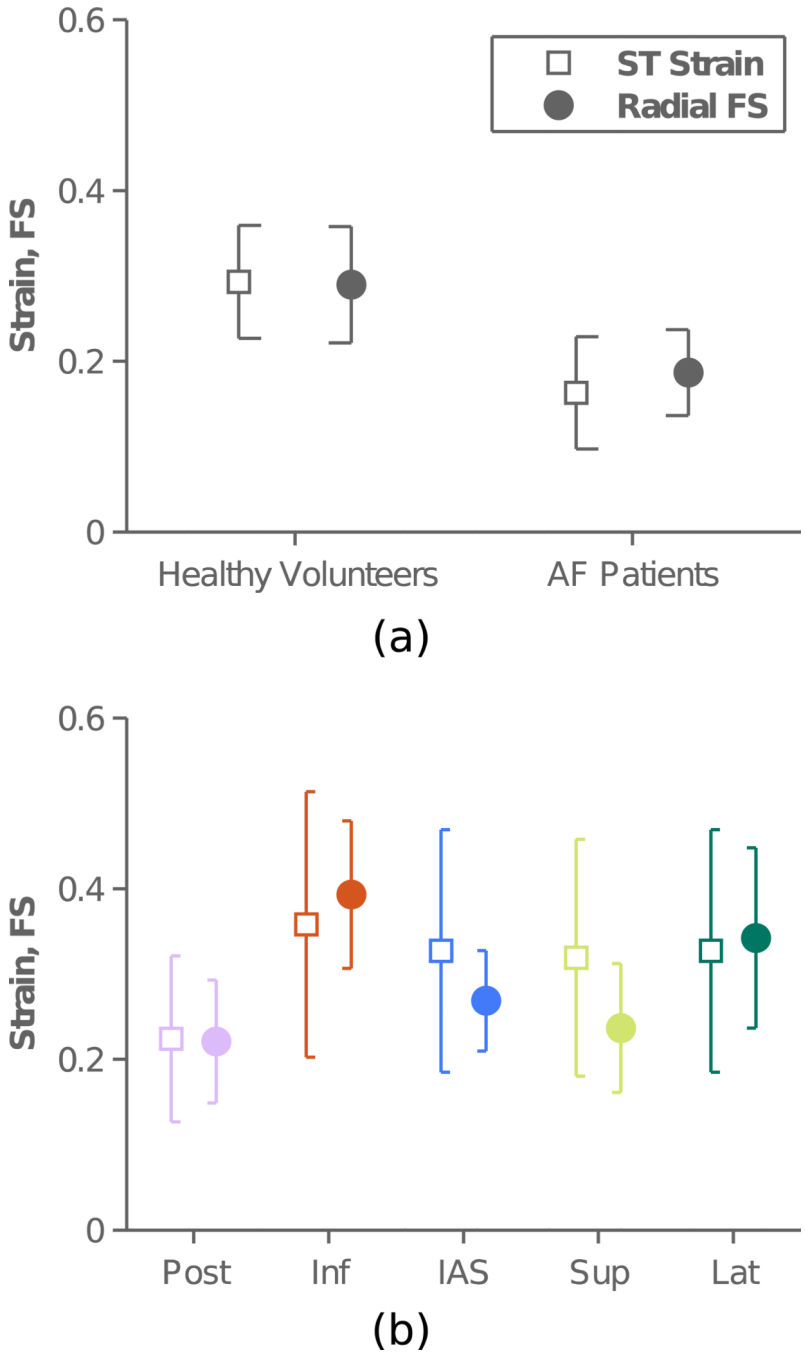

Figure 9.

Radial fractional shortening (Radial FS) compared to speckle-tracking wall strain (ST Strain). Error bars represent mean±SD. (a) We compared the average radial FS of healthy volunteers to [44] and of AF patients to [47], averaged over the entire left atrial wall. (b) We compared regional radial FS to [46] based on speckle tracking strain measured in 5 separate regions.